Supplementary Information

Probing Ag filamentary networks in a neuromorphic device using surface-enhanced Raman scattering

*Tejaswini S. Rao[1], Giridhar U. Kulkarni[1,]**

[1]Chemistry & Physics of Materials Unit, Jawaharlal Nehru Centre for Advanced Scientific Research, Jakkur P.O., Bangalore-560064, India

** Corresponding Author & Email Address: Prof. Giridhar U. Kulkarni (kulkarni@jncasr.ac.in)*

Table of contents

Table S1: Comparison table of techniques used to probe conductive Ag filamentary pathways in Ag-based devices

Device geometry (vertical/ lateral)	Device structure/ Active material	Technique used	What it probed	Requires special sample preparation	Invasive / non invasive	In situ/ ex situ/ in operando	Ref
Vertical	α-Si/Ag/Cu	C-AFM	multiple and spatially distributed conductive filaments	No	Non invasive	In situ	[1]
Lateral	Ag/CuO nanowires/ Au	TEM	direct evidence of Ag^+ ion migration and conductivefilament formation, governed by electrochemical metallization, the interplay of intrinsic defects, such as axial grain boundaries, with Ag nanoparticle nucleation, underscoring their critical role in facilitating filament growth	Yes	Invasive	In situ	[2]
Lateral	Au/Ag@TiO_2 nanowire networks/ Au	Infrared thermography	fundamental aspects of signal transmission in neuromorphic nanowire networks as a result of pathway formation between different electrodes	No	Non invasive	In operando	[3]
Lateral	Ag nanowire network	Infrared thermography	geometrically quantized percolation phenomenon via thermal/ electrical activation at the scale of the whole network (several millimeters)	No	Non invasive	In operando	[4]

Lateral	Au/MoS_2/Ag	TEM	evolution dynamics of conductive filaments in planar ECM memristors	Yes	Invasive	In situ	[5]
Vertical	Au/polyvinylimidazole/Ag/Au	Impedance spectroscopy	ionic/ electronic transfer characteristics of the device	No	Non invasive	In operando	[6]
Lateral	Au/Ag nanostructures/Au	COMSOL Simulations	anticipated percolation path with electric field application	Not applicable	Not applicable	Not applicable	[7]
Lateral	Au/Ag nanostructures/Au	Impedance Spectroscopy	stochastic resistive switching, and contribution of resistive, capacitive, and diffusion components for percolation path formation	No	Non invasive	In operando	[8]
Lateral	W/Ag nanoclusters in SiO_2 matrix/Au	TEM	fundamental electrochemical dynamics of metal inclusions inside conventional solid-state dielectrics	Yes	Invasive	In situ	[9]
Lateral	Ag nanowires	Electrical resistance tomography	map the conductivity distribution in nanowire networks, and to image and track, over time, the evolution of potentiated localized regions in memristive samples exhibiting conductivity	No	Non invasive	In situ	[10]

			plasticity				
Lateral	Au/Ag nanostructures/Au	SERS	ascertaining the electric field induced morphological changes in the Ag nanostructures	No	Non invasive	Ex situ	**Present work**

A comparison of different techniques employed for probing Ag conductive filament formation in Ag-based two-terminal devices is presented in Table S1. From the literature surveyed, it can be observed that SERS has not been utilized as a tool for gaining insights into the electric-field induced morphological changes. Therefore, SERS, being a non-invasive technique requiring minimal sample preparation, offers a promising approach for ex situ observation of the morphological changes.

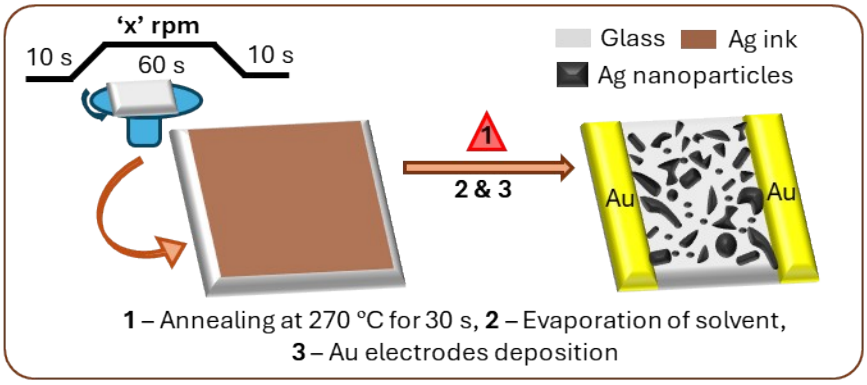

Figure S1 Schematic of the Ag-ASN device fabrication protocol.

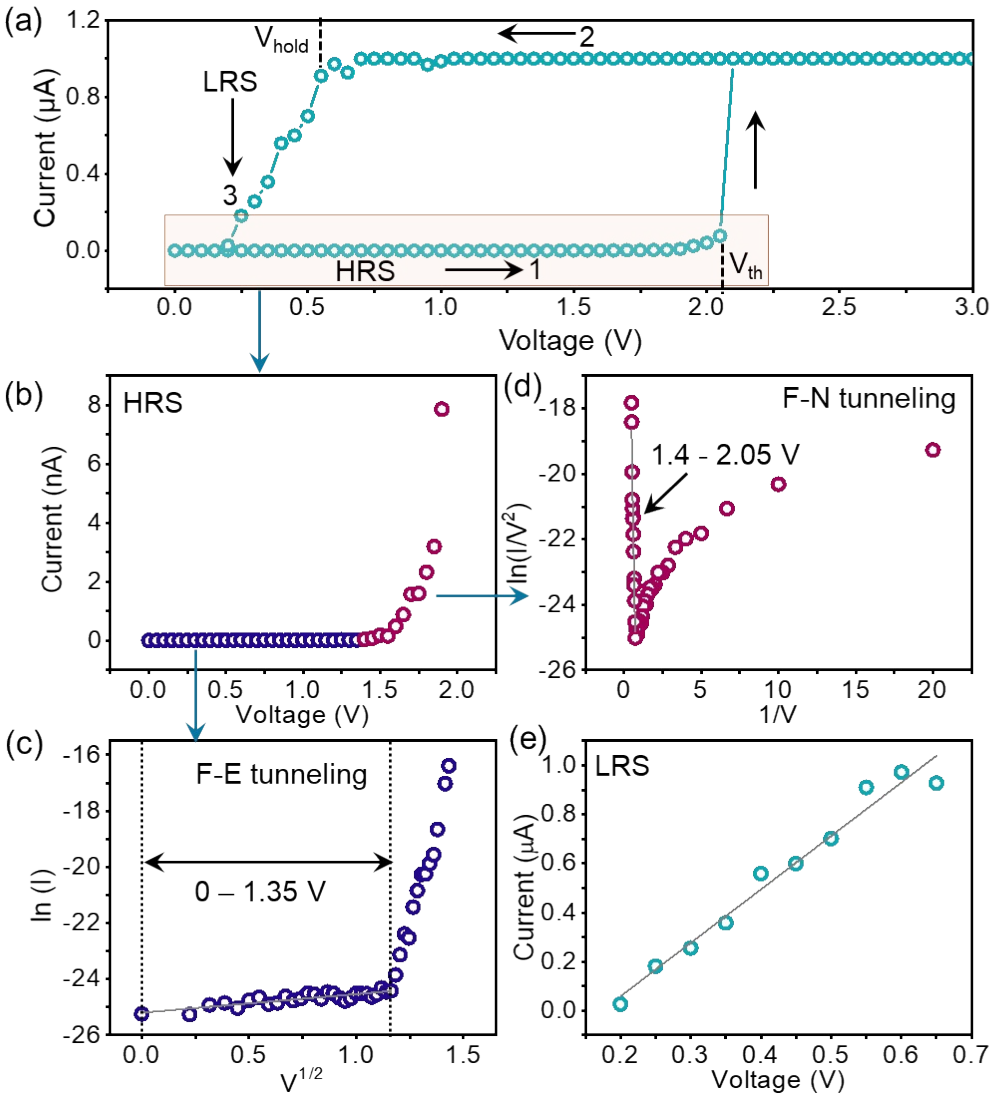

Figure S2 (a) I-V sweep considered for understanding the current transport in the HRS and the LRS. (b) Magnified I-V sweep in the HRS during the forward sweep (colored region in (a)). HRS from 0-2.05 V during the forward sweep replotted as (c) ln(I) versus $V^{1/2}$ using equation 1 showing F-E tunnelling from 0 to 1.35 V (d) $\ln(I/V^2)$ versus 1/V using equation 2 showing F-N tunnelling from 1.4-2.05 V. (e) Linear relation between current and voltage showing an ohmic behavior in the LRS during the reverse sweep.

$$I \propto AT^2 \exp\left[-\frac{q\emptyset}{kT} + q\left(\frac{q^3V}{4\pi\varepsilon}\right)^{\frac{1}{2}}\right] \quad [1]$$

$$I \propto V^2 \exp\left[-\frac{kd}{V}\right] \quad [2]$$

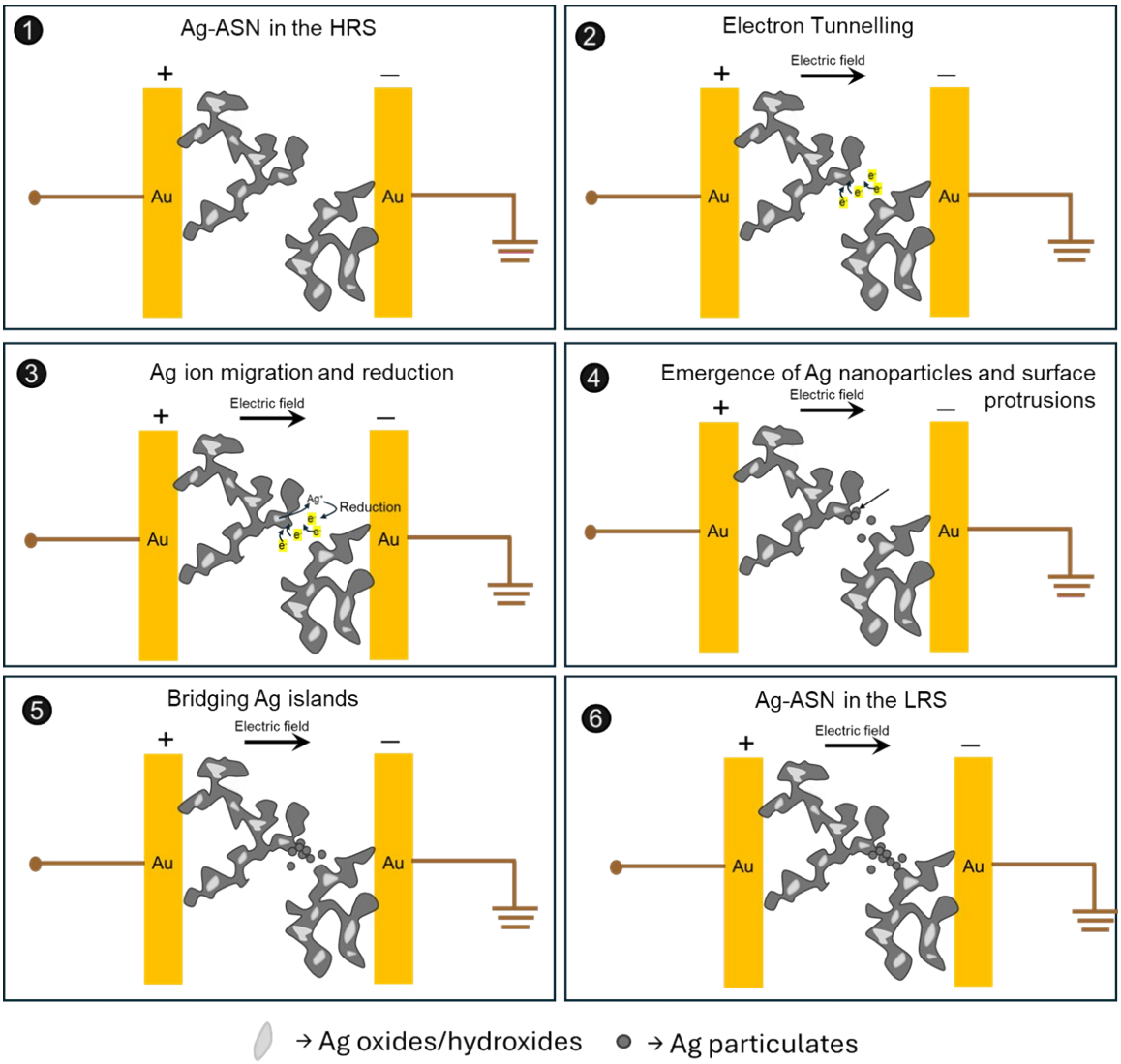

Figure S3 Schematic of the switching mechanism – (1) initially, the Ag-ASN device is in the HRS, (2) – with the application of electric field, F-E, F-N tunneling occur, (3) – the Ag^+ ions drift along the Ag islands followed by reduction, (4) – leading to nucleation and emergence of nanoparticles, and protrusions, (5) – bridging the Ag islands, and (6) switching the device to the LRS.

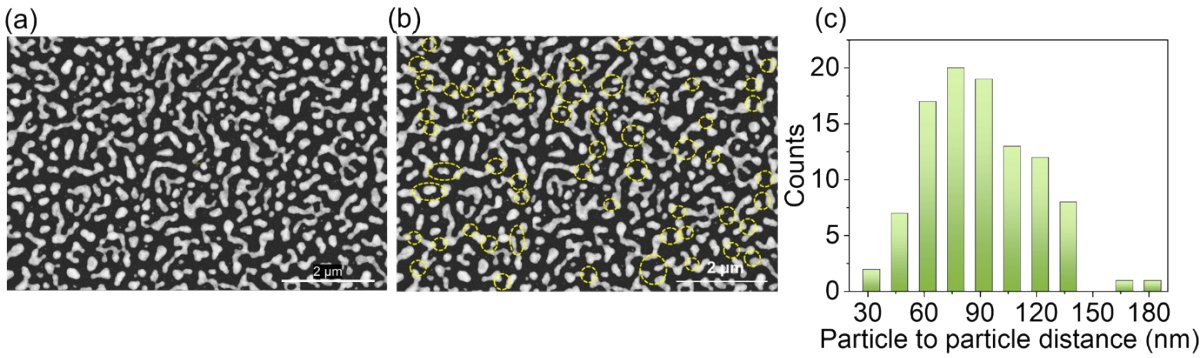

Figure S4 (a) FESEM image used for COMSOL simulations. (b) Regions of sharp curvatures marked with yellow dotted circles. (c) Histogram showing the distribution of inter-structure distances.

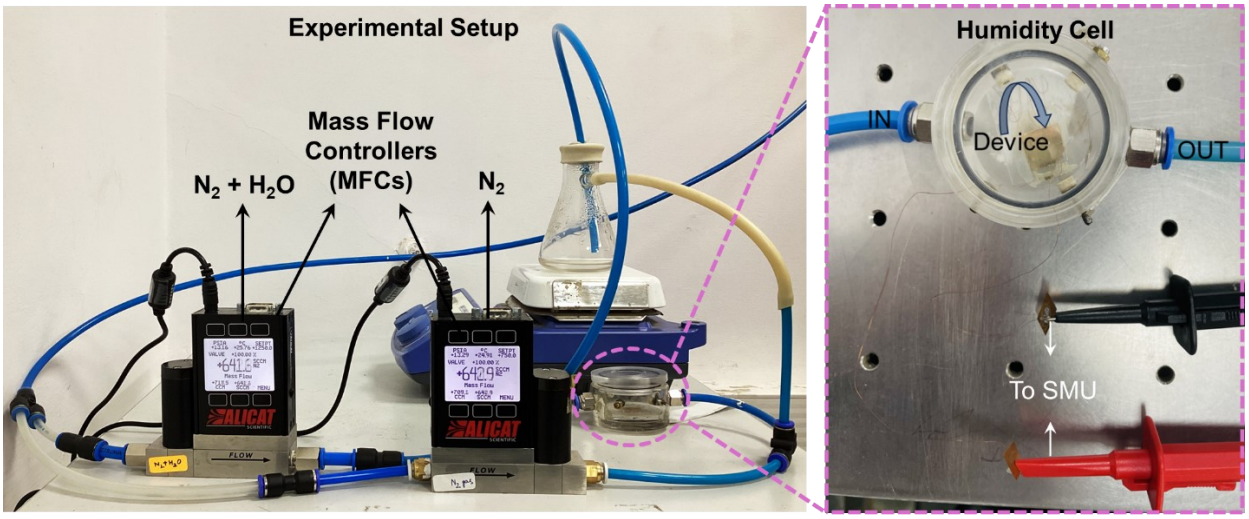

Figure S5 Photograph of the experimental setup developed in-house for maintaining a particular humidity inside the humidity cell containing the device. Photograph of the device placed in the humidity cell with inlet and outlet for gas flow and the copper wire connections to the SMU for electrical measurements (right).

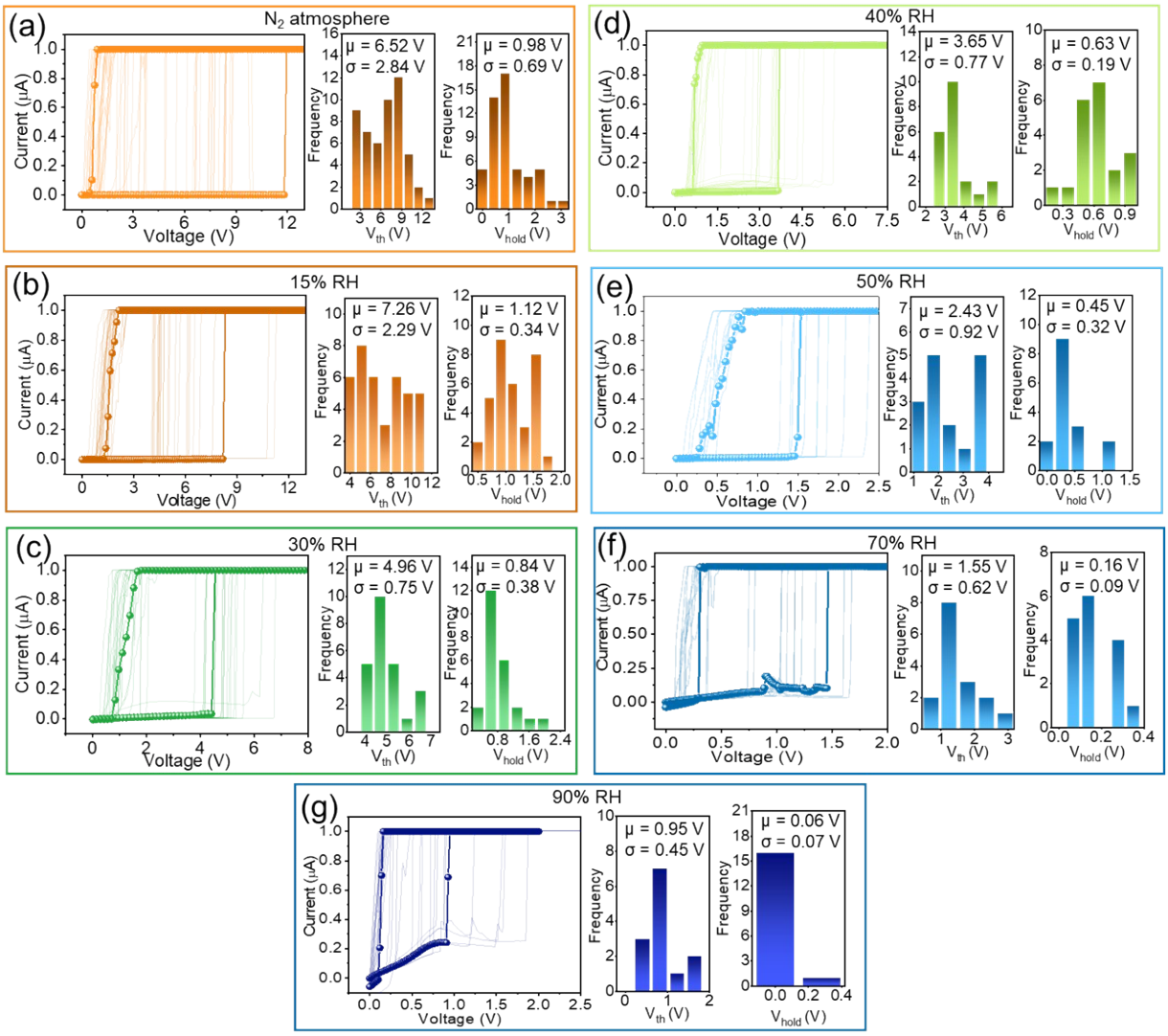

Figure S6 Switching characteristics of the device under different RH conditions. One of the representative I-V sweeps among several is highlighted for the sake of clarity. Histograms show the variation of V_{th} and V_{hold} under various RH conditions. The mean μ and deviation σ are mentioned in the inset.

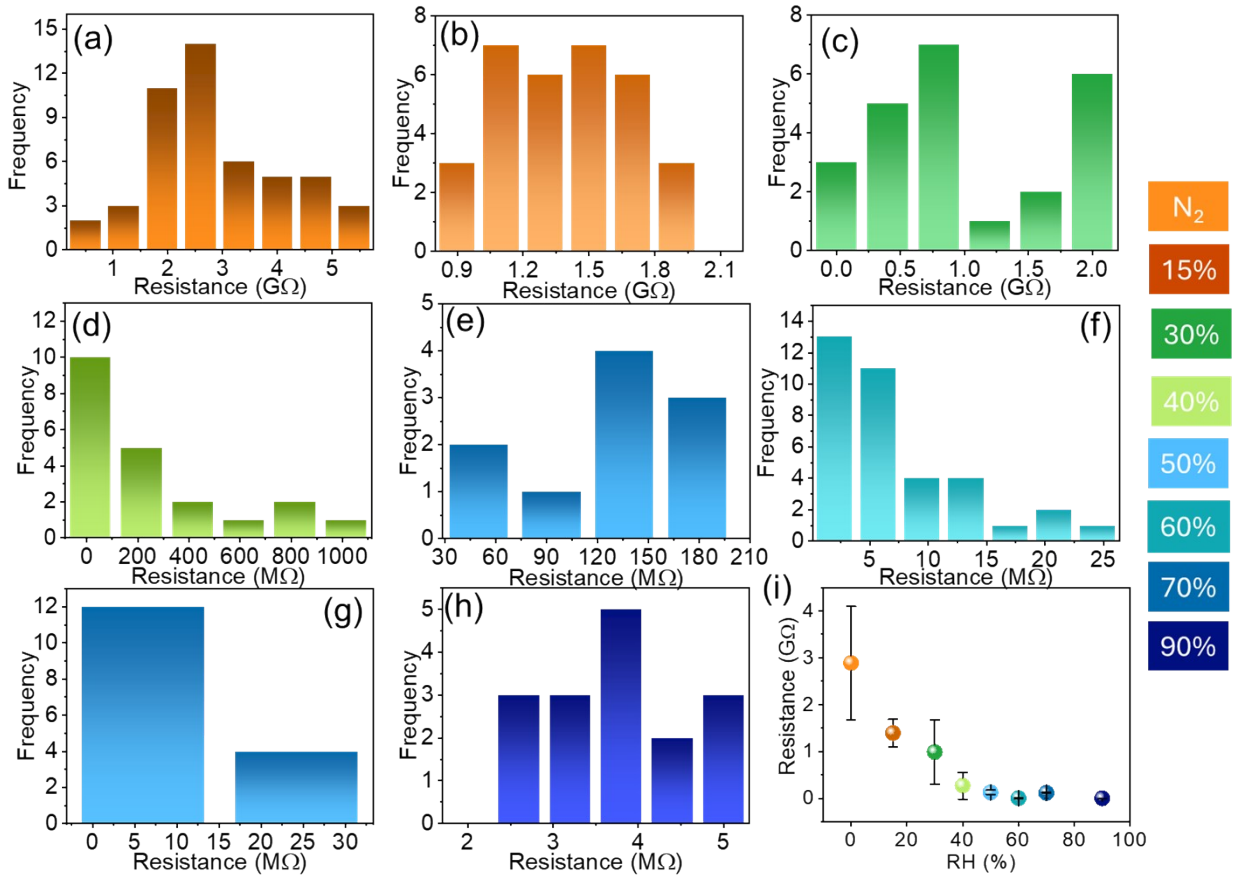

Figure S7 (a-h) Histograms showing the distribution of HRS at different RH. The HRS is measured at 0.1 V during the reverse sweep. (i) Variation of resistance with RH.

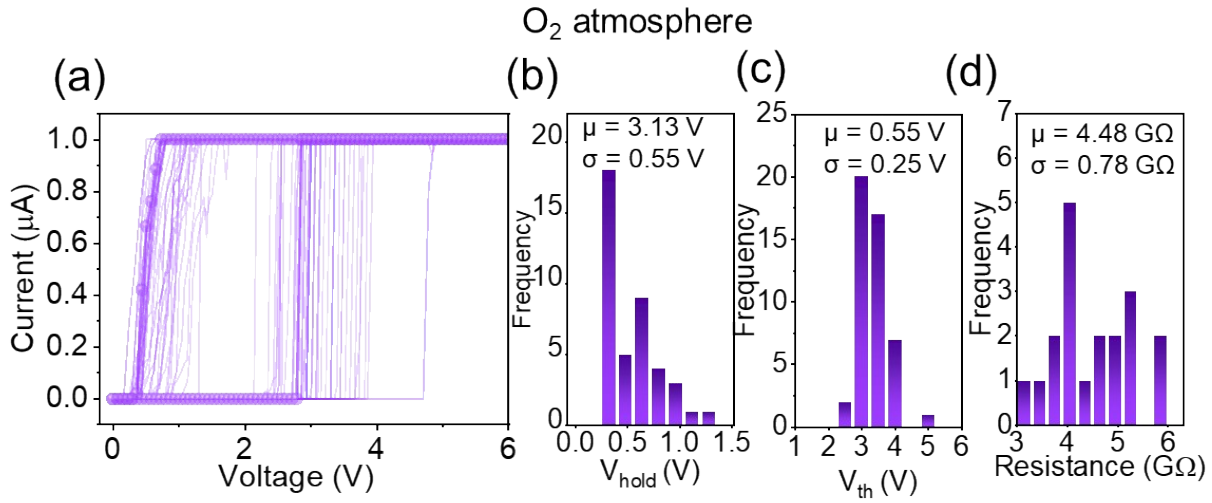

Figure S8 O_2 atmosphere (a) Switching behavior with one I-V sweep highlighted for clarity. Distribution of (b) $V_{th,}$ (c) $V_{hold,}$ and (d) HRS for ~ 35 I-V sweeps.

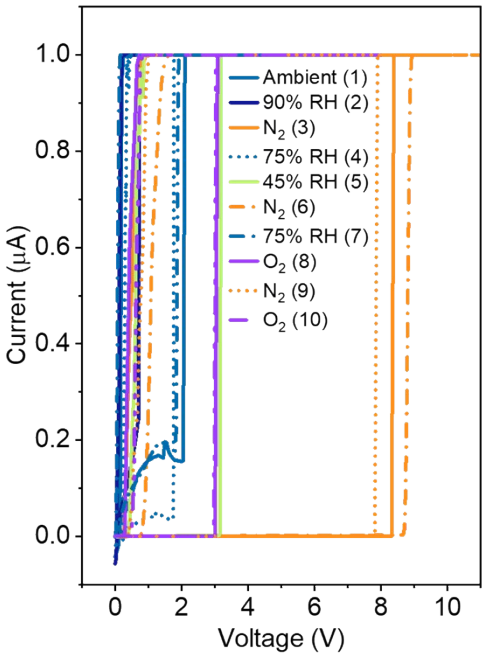

Figure S9 Switching behavior of the device when randomly cycled between different atmospheres and RHs. The numbers 1 to 10 indicate the order of cycling between atmospheres.

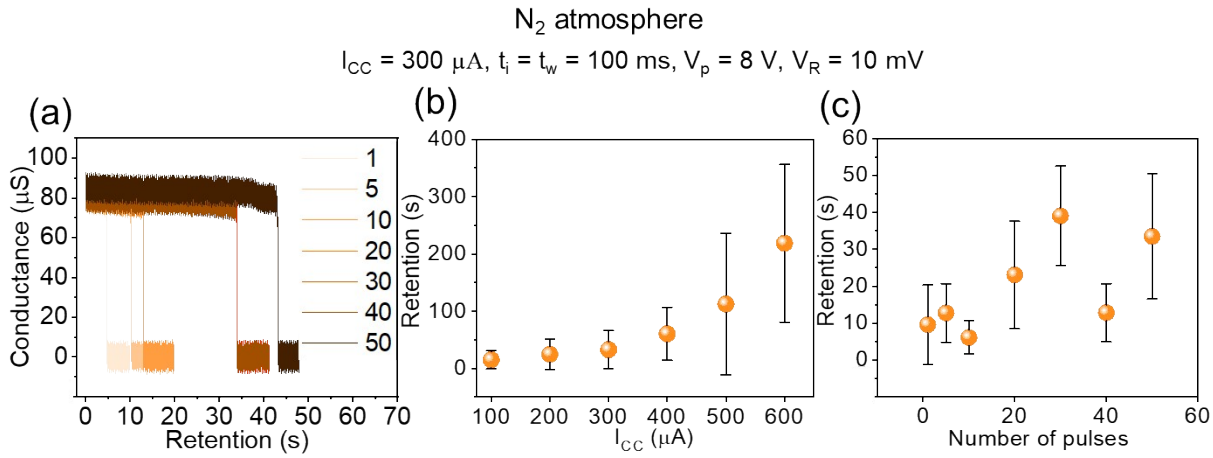

Figure S10 N_2 atmosphere (a) Retention of a G state achieved post-pulsing for varying number of pulses in the N_2 atmosphere. Variation of (b) G and (c) t_r with the increase in the number of pulses. Error bars are based on 5 measurements.

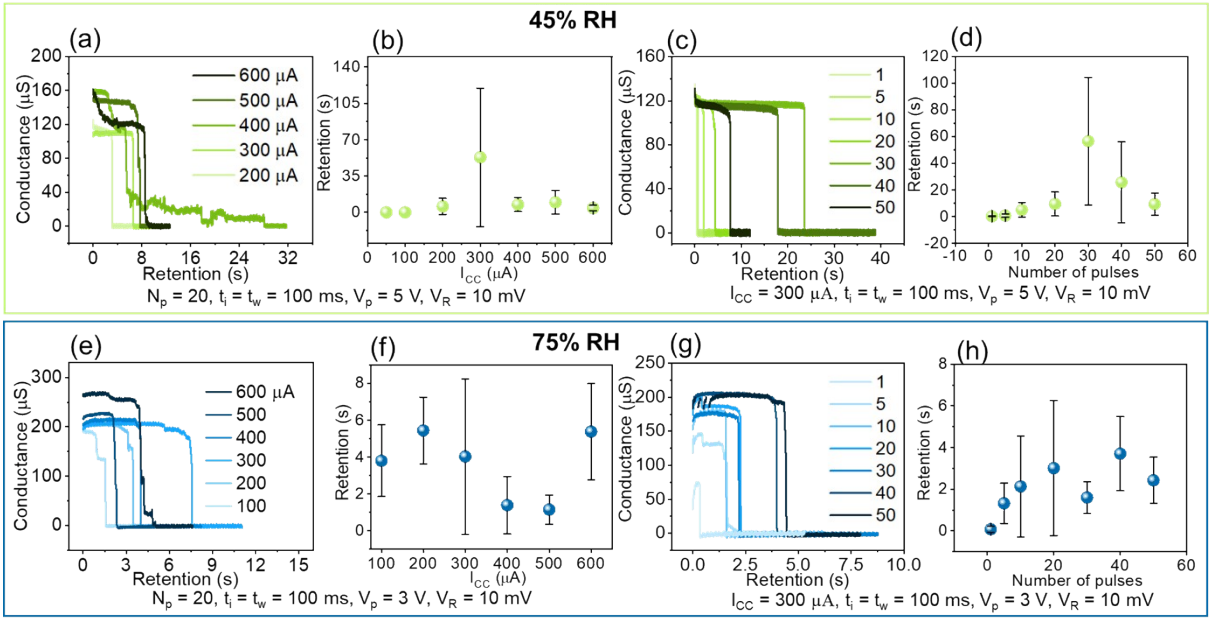

Figure S11 Retention of a G state achieved post-pulsing for varying (a, e) I_{CC} and (c, g) number of pulses at 45% and 75% RH, respectively. Variation of t_r with increasing (b, f) I_{CC} and (d, h) the number of pulses at 45% and 75% RH, respectively. Error bars are based on 5 measurements.

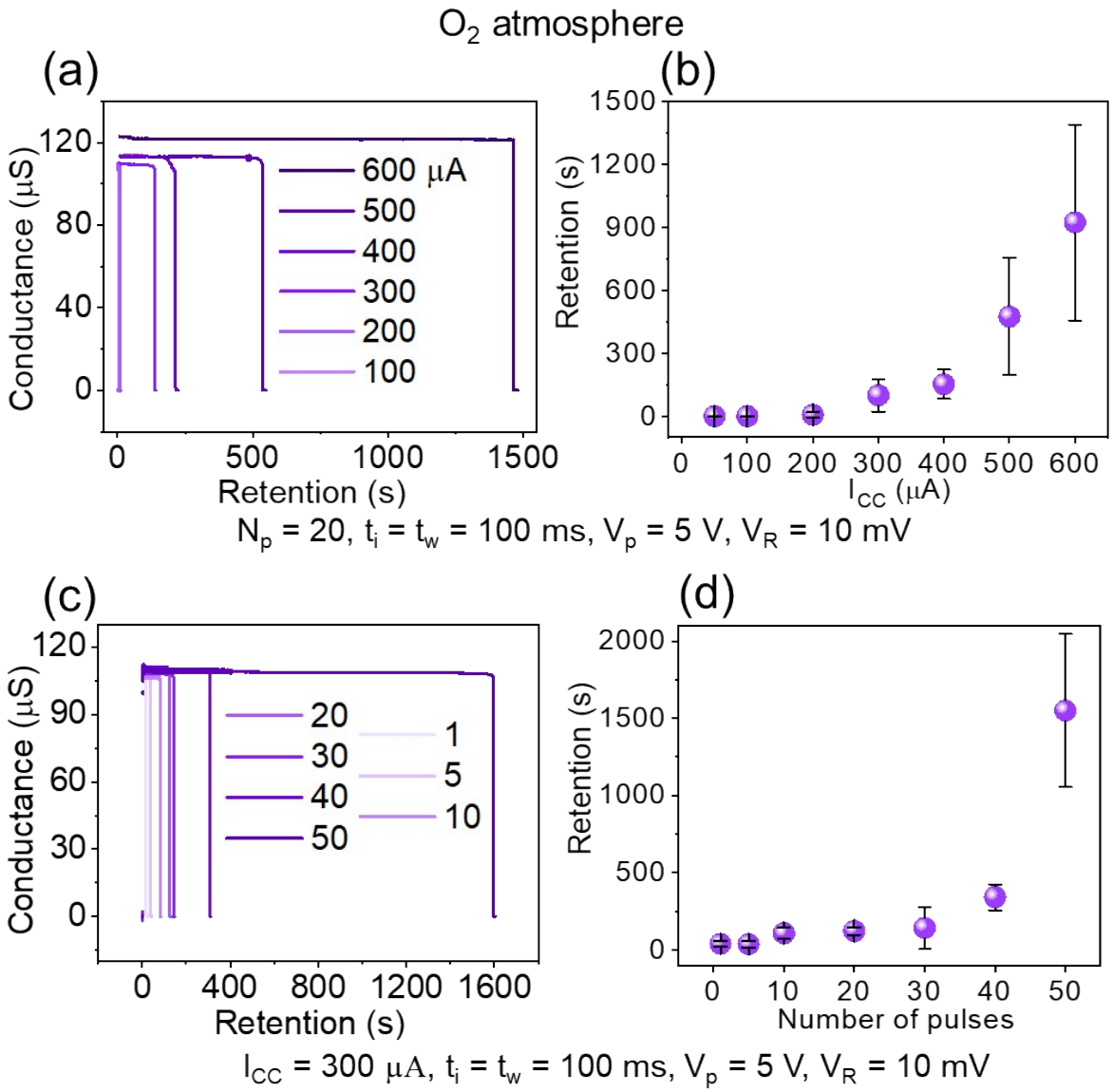

Figure S12 O_2 atmosphere. Retention of a G state achieved post-pulsing by varying (a) I_{CC} and (c) number of pulses. Variation of t_r with increasing (b) I_{CC} and (d) the number of pulses. Error bars are based on 5 measurements.

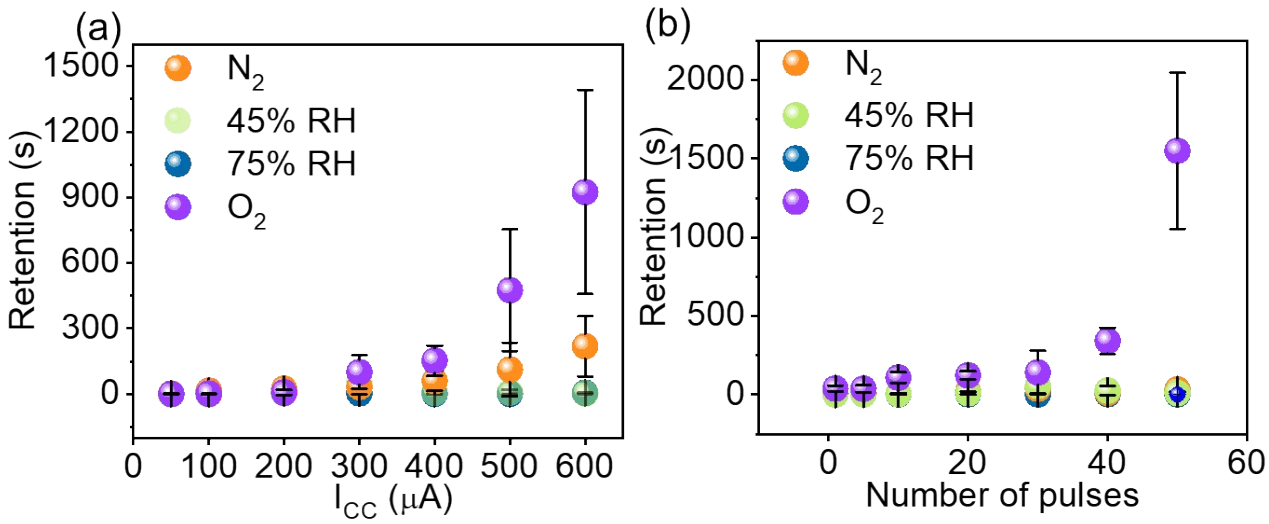

Figure S13 Summary of the pulsing behavior of the device in N_2, 45% RH, 75% RH, and O_2. Variation in the t_r with (a) I_{CC} and (b) number of pulses (N_P). The number of pulses (N_P) in different conditions was varied from 1 to 50 at an I_{CC} of 300 μA, with other parameters being the same as with varying I_{CC}.

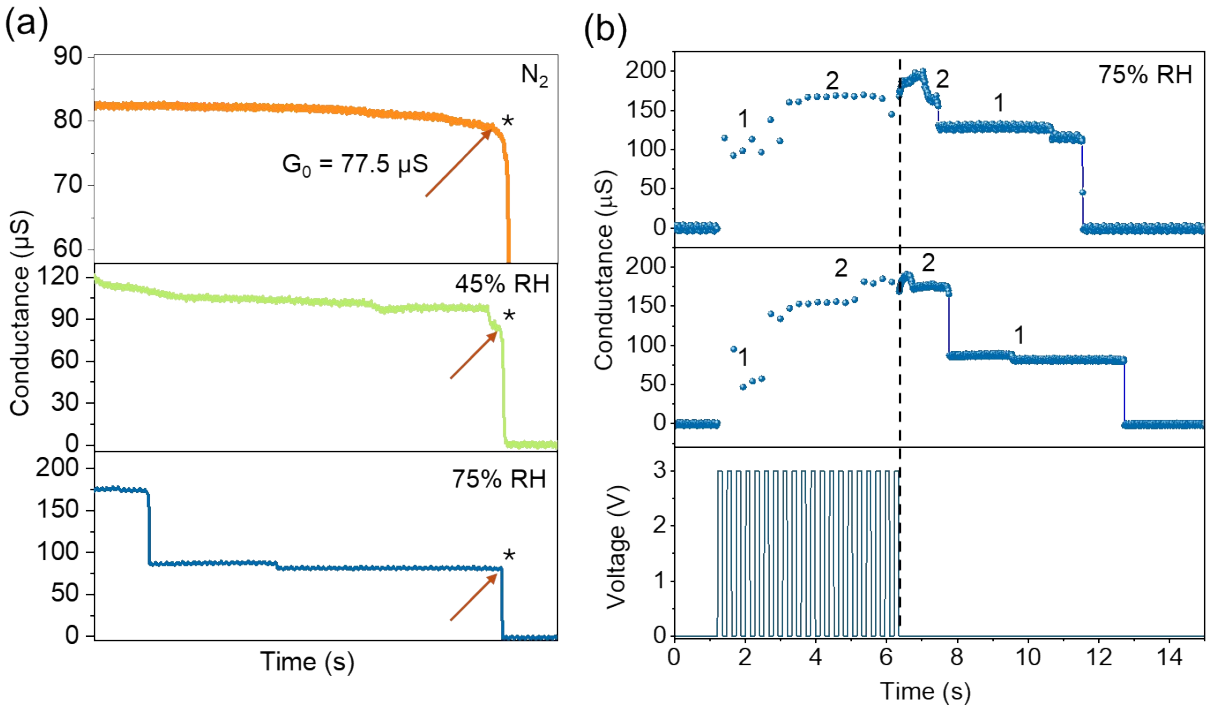

Figure S14 (a) Near quantum conductance values exhibited during retention in the N_2 atmosphere, 45% and 75% RH. (b) Bottom panel shows 20 voltage pulses (N_P) of 3 V amplitude (V_P) with t_i=t_w=100 ms. The top panels show the response of the device in 75% RH for the applied voltage pulses and the behavior after pulsing. Stages 1 and 2 during pulsing reflect the retention stages 1 and 2 after pulsing, suggesting that retention 1 is due to the state achieved at stage 1 during pulsing. It can be observed that state 1 achieved during pulsing is stabilized and retained for a longer time,

as can be seen from retention state 1. Hence, it can be hypothesized that the filaments formed during the initial stages of pulsing get stabilized and retained for a longer time than those formed during the later stages of pulsing.

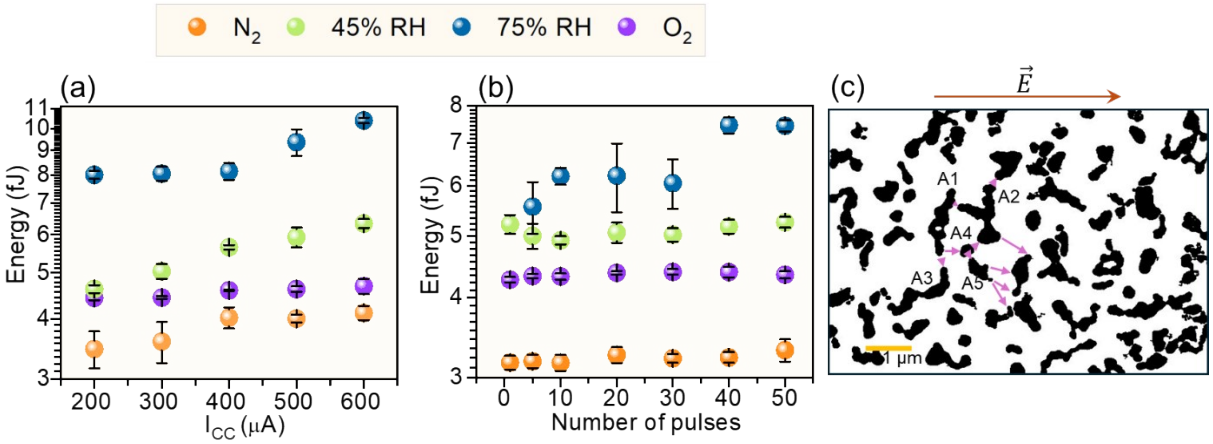

Figure S15 Energy consumption per synapse with varying (a) I_{CC} and (b) number of pulses in different atmospheres. (c) FESEM binary image of agglomerates in the Ag-ASN, analyzed using ImageJ software. Each agglomerate (approximately) can connect with 2 to 4 agglomerates in the direction of the electric field, indicated with arrow marks for agglomerates marked A1, A2, A3, A4, and A5.

Note S1

Energy consumption by a device was calculated using the equation: [7]

$E_{cons} = I \times V \times t$

$= G \times V_R \times V_R \times t_i$

Where G is the conductance state achieved post-pulsing, V_R is the reading voltage, t_i is the pulse interval.

The conductance values are taken from Figures 2e and f, V_R is 10 mV, and t_i is 100 ms.

However, to calculate energy consumption per synapse, 2 Ag agglomerates (area ≥ 0.03 μm^2) separated by the nanogap containing nanoparticles are considered as a single synapse.

Thus, the energy consumed to form a conduction path between 2 Ag agglomerates is calculated using the equations below;

Average Ag agglomerate density = ρ is 1 per sq. μm, which is ~1.5×10^9 per sq. inch.

Each Ag agglomerate has a possibility of connecting with 2 to 4 neighboring agglomerates approximately in the direction of the electric field, so n = 2 to 4 (see Figure S13c)

Average synaptic junction density = $N = \rho \times n = 3.1\times10^9$ per sq.inch

Energy consumed by a device $E_{cons} = G \times V_R \times V_R \times t_i$

Energy density $E_0 = E_{cons}/A$, where A is the area of the device 40×5000 $\mu m^2 \sim 3.1\times10^{-4}$ sq. inch

The fill factor of the Ag-ASN with only agglomerates is ~ 26%

Actual synaptic junction density $N_0 = N \times f = \rho \times n \times f = 0.8 \times 10^9$ sq.inch

Energy consumed per synapse $E_s = E_0/N_0 = (G \times V_R \times V_R \times t_i / A) / (\rho \times n \times f)$.[11]

Note S2

$$2H_2O \rightarrow O_2 + 4H^+ + 4e^- \quad \ldots(1)$$

$$Ag_2O\ (s) + 2H^+ \rightarrow 2Ag^+ + H_2O \quad \ldots(2)$$

$$Ag^+ + e^- \rightarrow Ag \quad \ldots(3)$$

(1) is the anodic half reaction, and (3) is the cathodic half reaction.

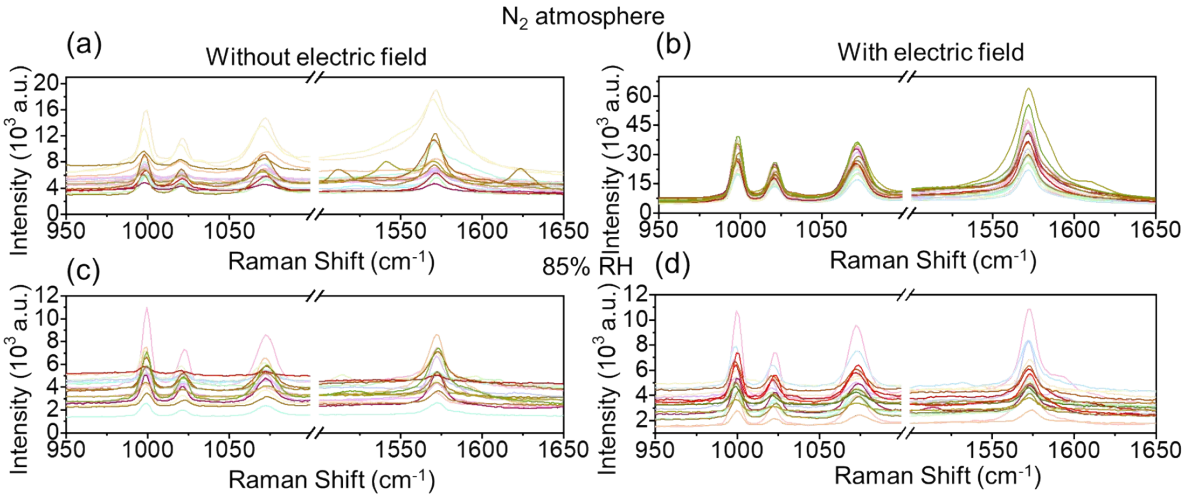

Figure S16 Raman spectra (λ=532 nm) (a, c) without (across D_{cd}) and (b, d) with (across D_{ab}) electric field application in the N_2 atmosphere, and 85% RH, respectively.

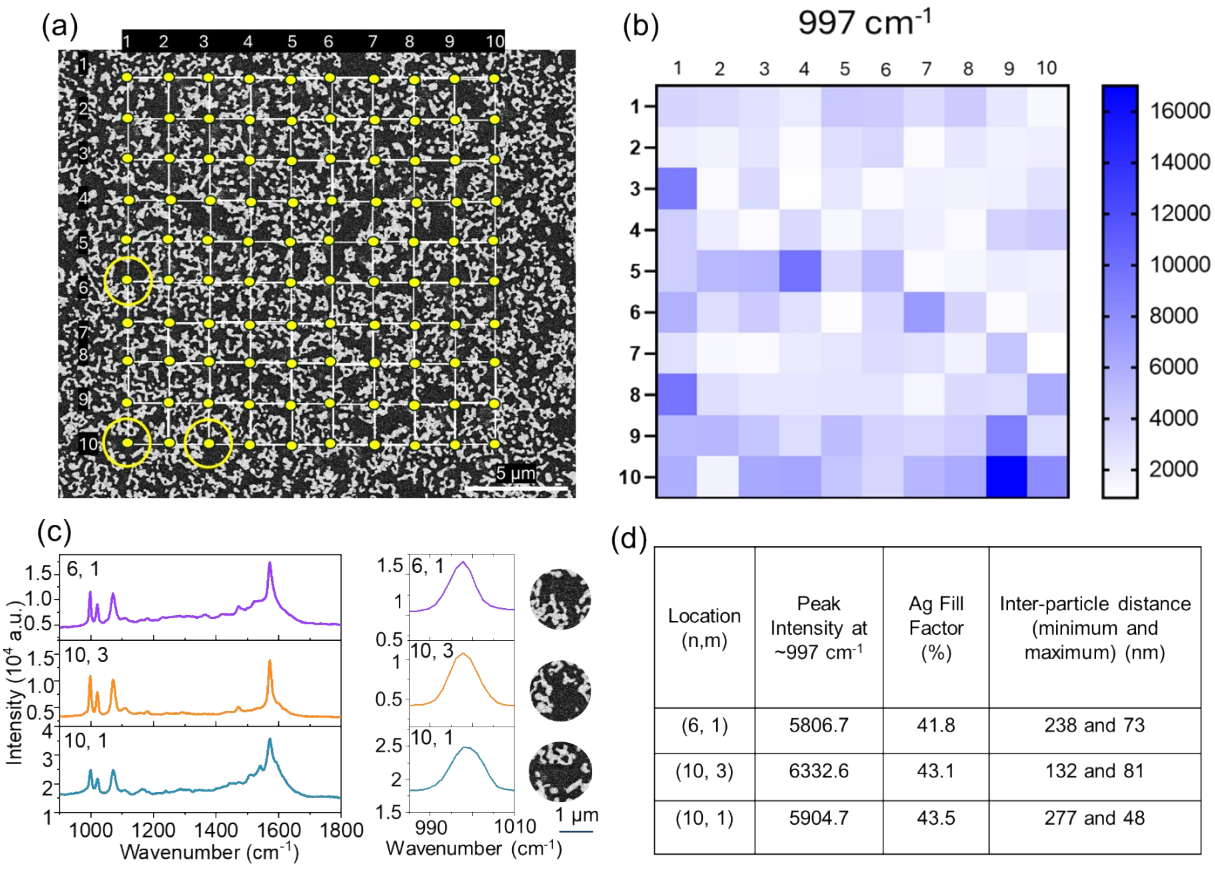

Location (n,m)	Peak Intensity at ~997 cm^{-1}	Ag Fill Factor (%)	Inter-particle distance (minimum and maximum) (nm)
(6, 1)	5806.7	41.8	238 and 73
(10, 3)	6332.6	43.1	132 and 81
(10, 1)	5904.7	43.5	277 and 48

Figure S17 (a) FESEM image with a grid of yellow dots each representing the centre of the region used for collecting the Raman spectra, and the big yellow circles mark the regions among them, exhibiting similar Raman signal intensities. (b) Pixelated view of the variation in the Raman peak intensity at ~997 cm^{-1}. Scale bar represents the Raman intensity counts. (c) Raman spectra at three different locations mentioned in the inset showing similar Raman signals (left). Magnified view of the peak at ~997 cm^{-1} (middle). FESEM images at the mentioned locations (right). (d) Tabulation of Raman and morphological parameters at the three locations.

Raman signals were obtained from different regions of the same Ag-ASN sample (see the FESEM image in Figure S17a overlaid with a data collection grid). We observe a spatial variation in the signal intensities of the characteristic thiophenol peak at ~997 cm^{-1} (see the color mapping in Figure S17b). For comparison, three spectra were considered with similar peak intensities, and their morphological parameters obtained through FESEM images were compared (see spectra and FESEM images in Figure S17c). The laser spot from the Raman spectrometer with a 50x objective covers ~3 μm^2 area. Accordingly, the morphological regions were identified. The locations (6, 1) and (10, 1) showed similar peak intensities. The microscopic image analysis from these regions gave similar fill factors (area of Ag coverage) and range of inter-particle distances. At location (10, 3), the Raman peak intensity was slightly higher, which was also reflected in its inter-particle distance, though the fill factor was comparable with that at locations (6, 1), and (10, 1) (see table

in Figure S17d). These observations show that inter-particle distances play an important role in determining SERS signal intensities. The variations in the peak intensities can also arise from the analyte molecule distribution, sharp curvatures on the Ag islands/particles, and the proximity of hotspots (if the inter-particle distance is less, the possibility of hotspots in proximity is higher).

Note S3

SERS Factor Calculation

The enhancement factor is calculated using the formula.[12]

$$SERS\ Factor = \left(\frac{I_{SERS}}{I_{Norm}}\right)\left(\frac{N_{Bulk}}{N_{Surf}}\right)$$

Where,

I_{SERS} is the intensity of the specific band in the SERS spectra

I_{Norm} is the intensity of the specific band in the normal Raman spectra of the analyte molecule

N_{Bulk} is the number of probe molecules illuminated under the laser beam in the bulk

$N_{Bulk} = \frac{A \times h \times \rho}{m}$ where A is the laser spot size, h is the penetration depth (100 µm), ρ is the density of thiophenol (1.08 g/cm^3) and m is the molecular weight of thiophenol (110.19 g/mol)

N_{SERS} is the number of probe molecules illuminated under the laser beam in the SERS experiments

$N_{SERS} = C \times A$ where C is the surface density of thiophenol (6.8×10^{14} molecules/cm^2), A is the laser spot size

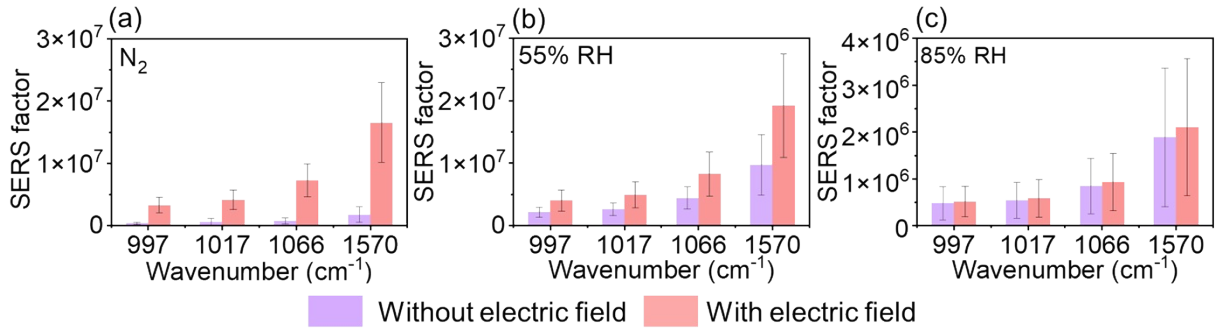

Figure S18 SERS factor of the prominent thiophenol peaks without and with electric field application in the (a) N_2 atmosphere, (b) 55%, and (c) 85% RH. Error bars are derived from 99 spectra along the device length.

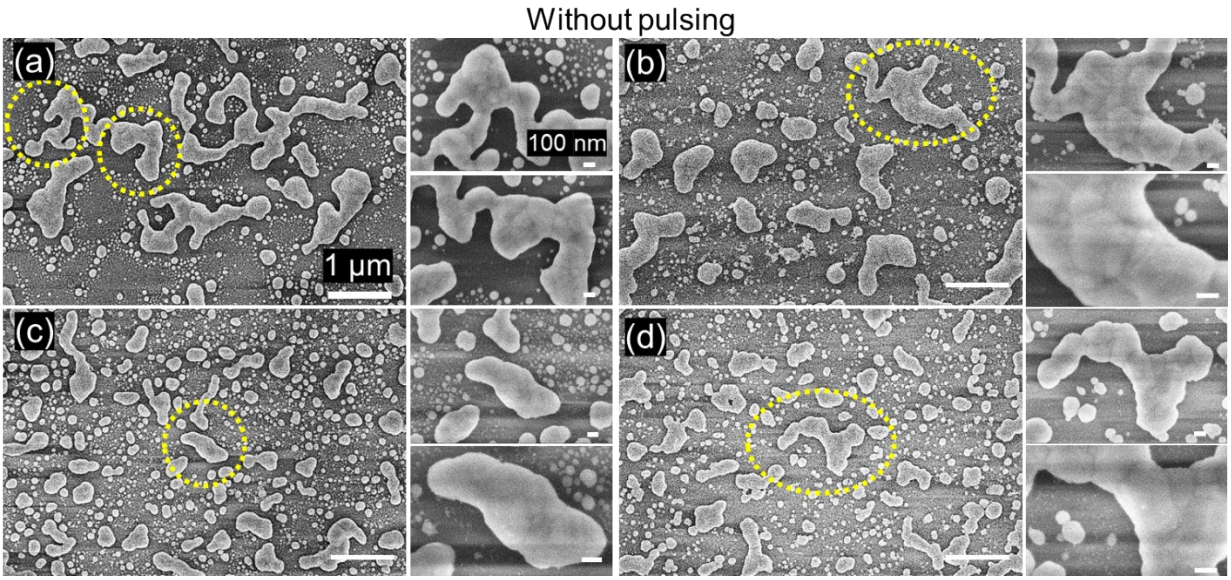

Figure S19 FESEM images in D_{cd} without pulsing treatment, where yellow circles show the region magnified on the right in (a) the N_2 atmosphere, (b) at 55% RH, (c, d) at 85% RH. Scale bar in (a) applies to all the figures.

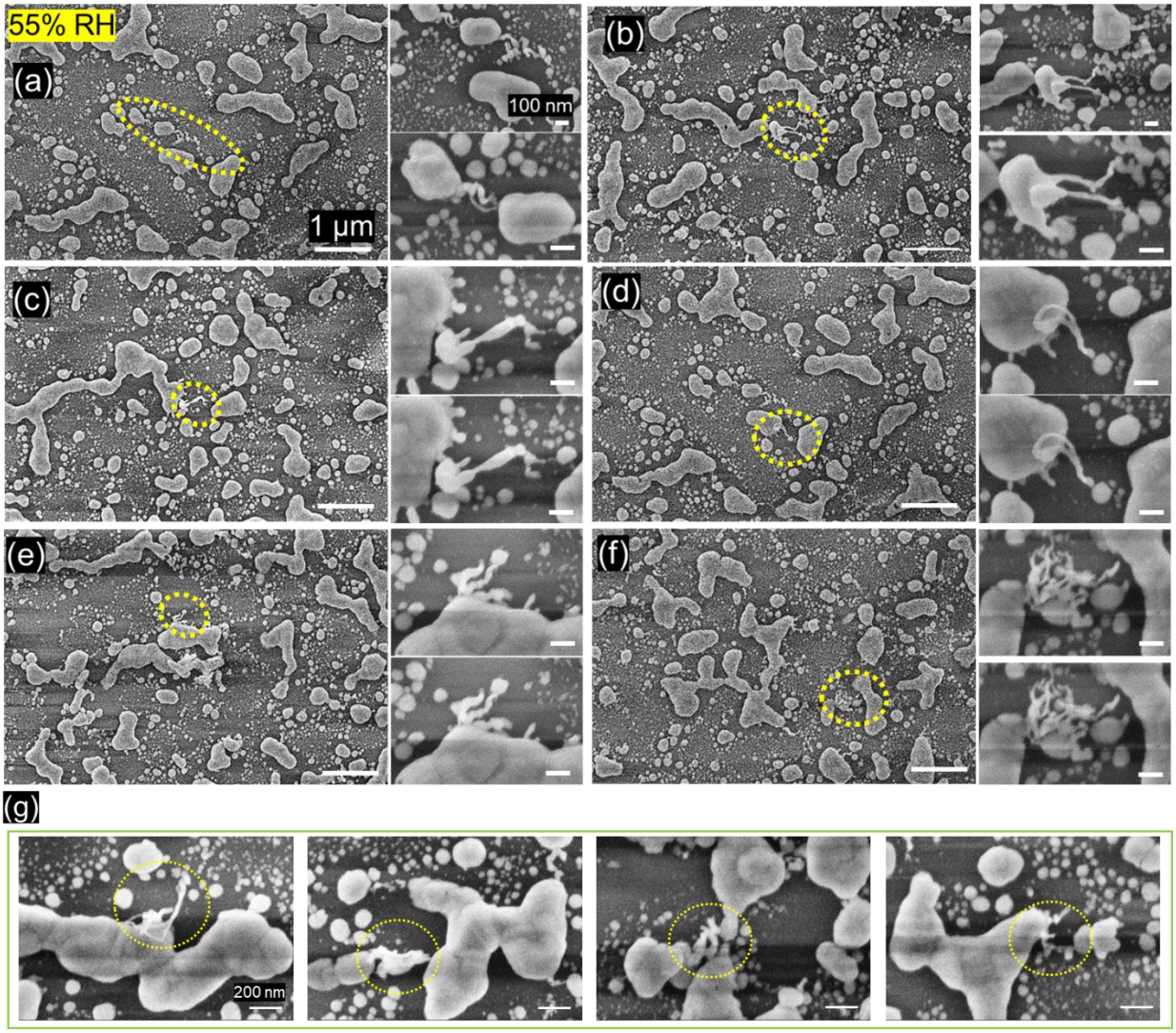

Figure S20 FESEM images in D_{ab} with electric field treatment at 55% RH, with magnified images showing the protrusions on the Ag structures and directed conduction paths. The scale bar in (a) applies to others. (g) Magnified FESEM images showing protrusions.

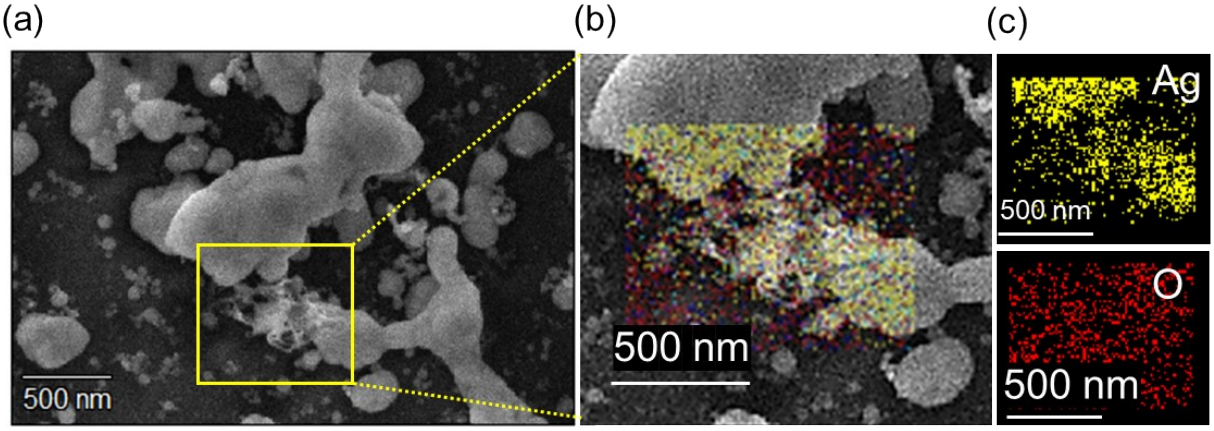

Figure S21 (a) FESEM image showing the dendritic/hairy growth between Ag particles. (b) EDS color mapping showing the elemental composition in the marked region containing the hairy structure. (c) Elemental mapping showing the Ag and O composition in the marked region.

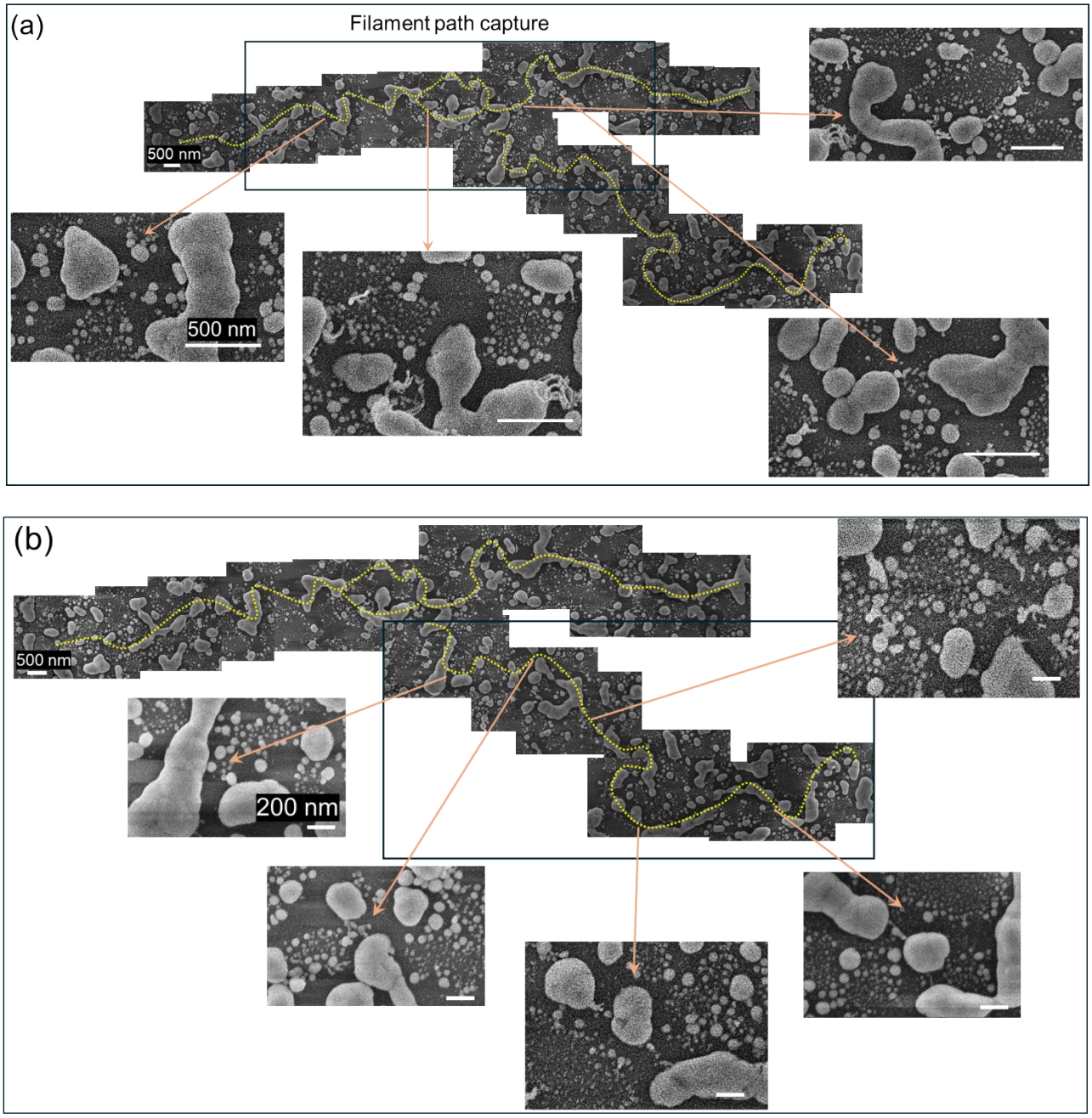

Figure S22 (a-b) Filamentary conductive paths in the device pulsed at 55% RH. Scale bar on one of the magnified images in (a) and (b) applies to all the images.

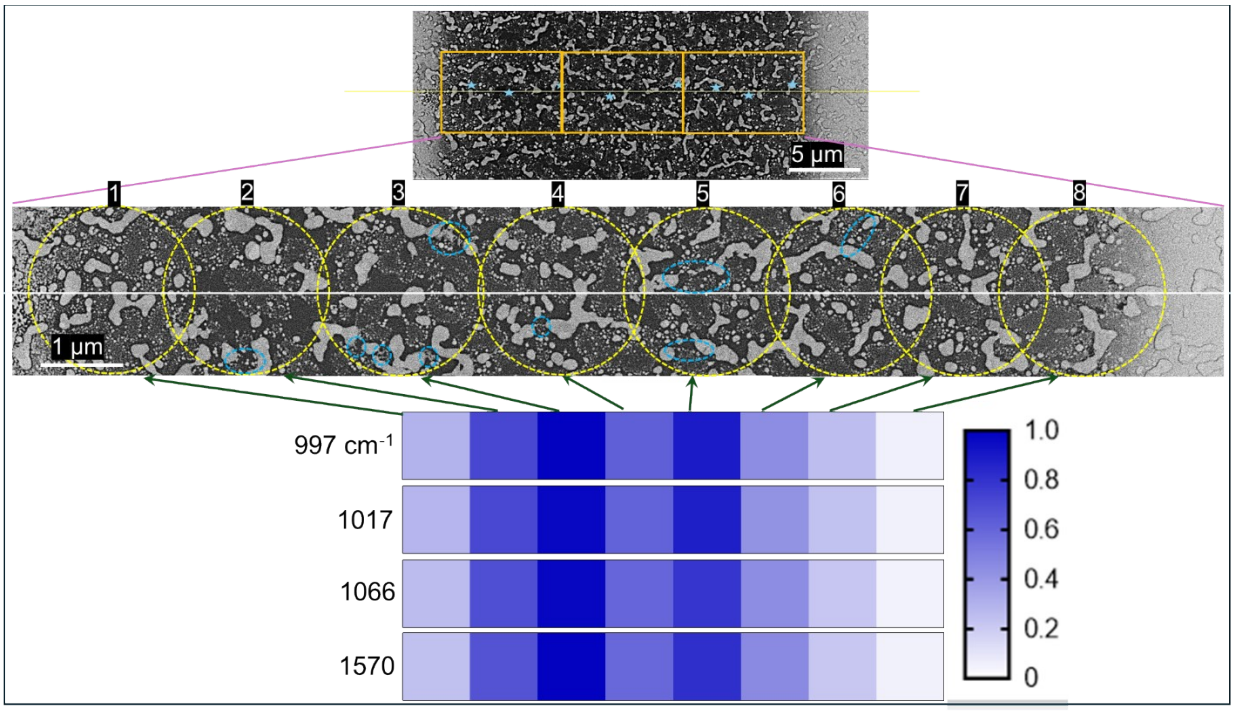

Figure S23 FESEM image of the region where the Raman spectra are captured after pulsing at 55% RH, with the star markers indicating the centre of the laser spot. Middle: magnified FESEM image with the dotted circles marking the region where the spectra have been captured. Bottom: the spectral color map corresponding to the marked regions of the prominent thiophenol peaks. Scale bar represents normalised Raman intensity counts.

The increased peak intensity in the pulsed device is correlated with the microscopic images to confirm the possible reason for the peak enhancement. Figure S23 shows the FESEM image of the region where the Raman spectra were captured, with the yellow dotted circles indicating the approximate region of the individual spectrum. The spectral color map shows the thiophenol peak intensity variation across the region. The blue dotted circles indicate the protrusions or paths created due to pulsing. Accordingly, regions 3 and 5 show the highest peak intensities, and it can be observed that there are more directed paths and protrusions in those regions, contributing to SERS hotspots possibly. This serves as evidence that the morphological change in the device is directly affecting the SERS intensity.

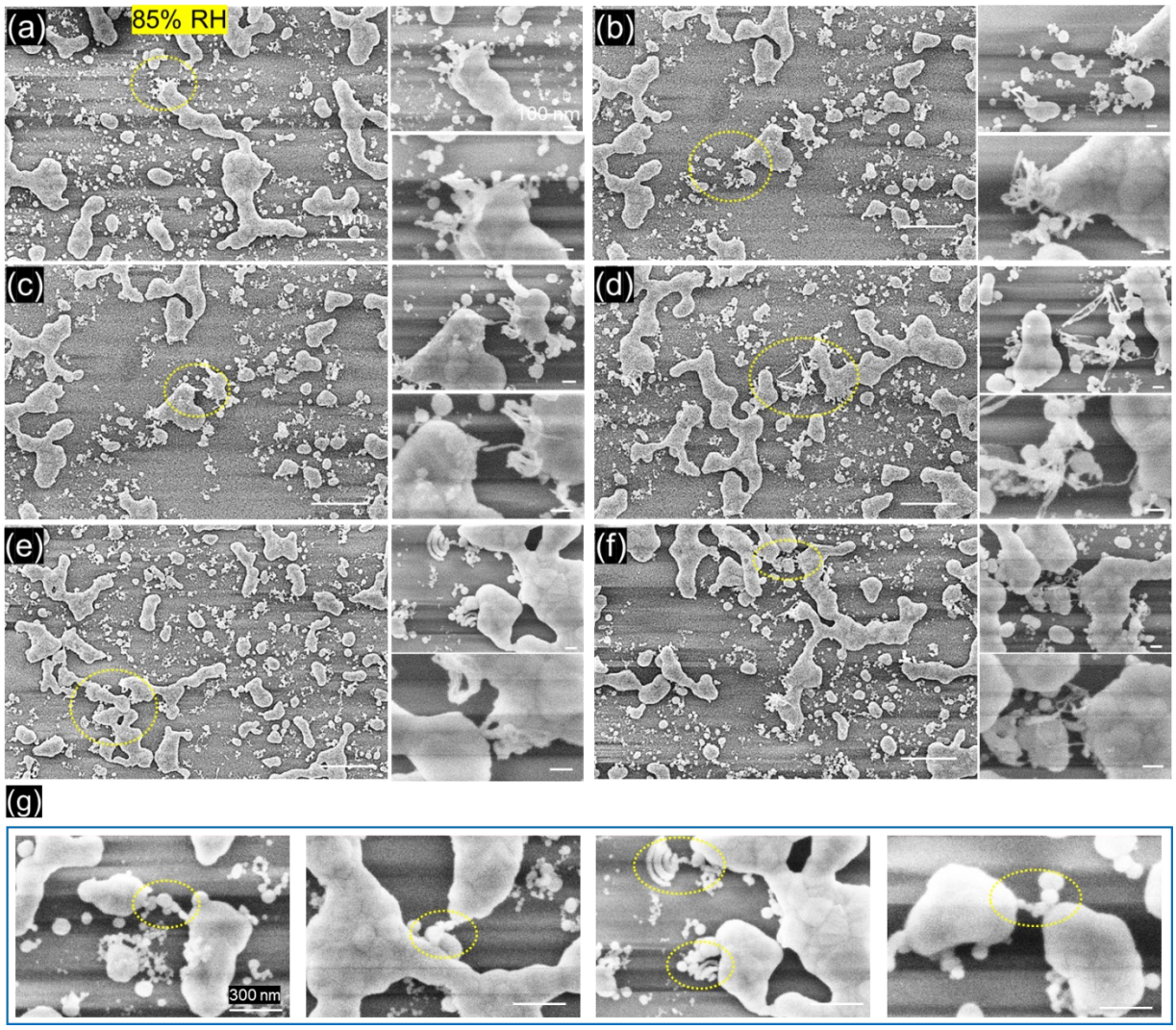

Figure S24 (a-f) FESEM images in D_{ab} with electric field treatment at 85% RH, with magnified images showing the protrusions on the Ag structures and directed filamentary paths. (g) Magnified FESEM images showing protrusions. Scale bar in (a) applies to all the other images.

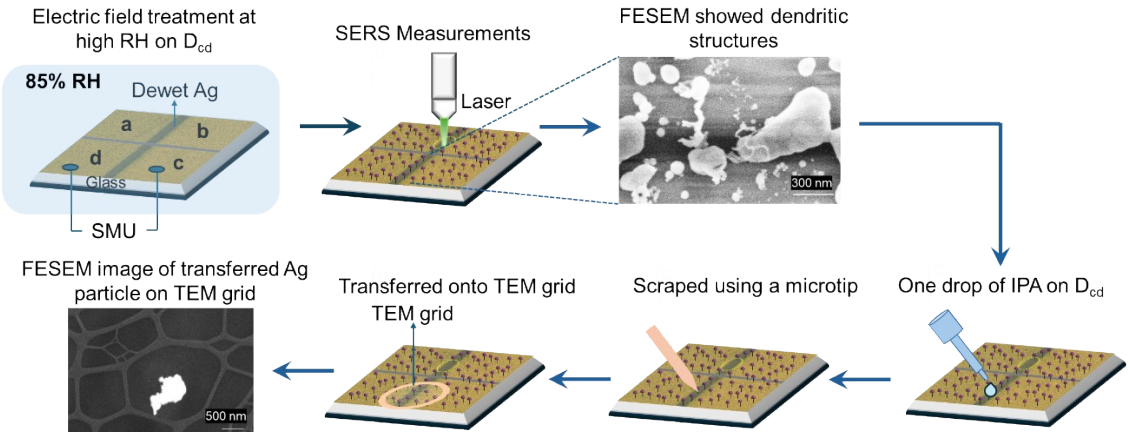

Figure S25 Sample preparation process for TEM characterization

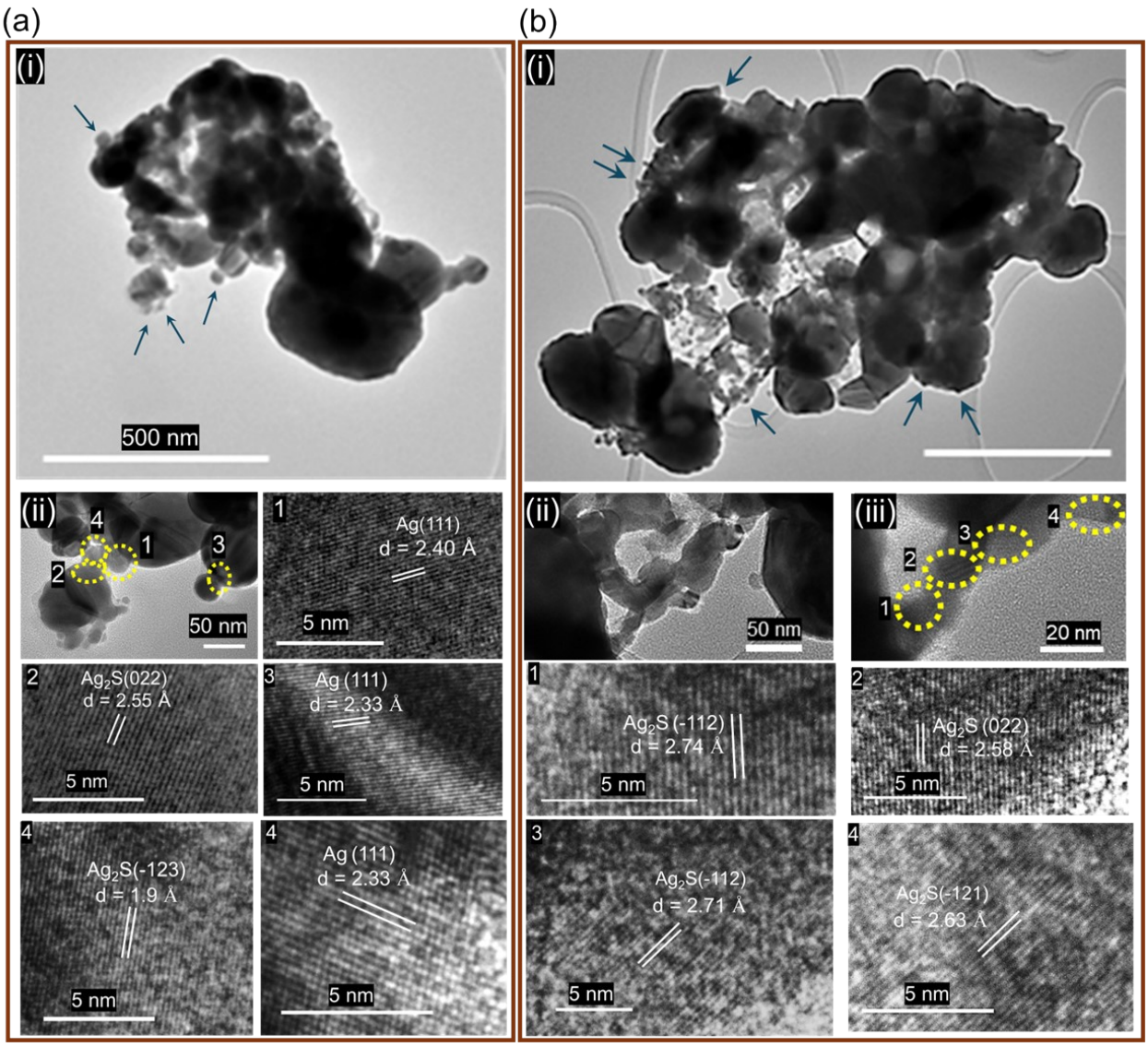

Figure S26 (a-i and b-i) TEM images showing the filamentary outgrowths marked with the blue arrows. The scale bar in (a) applies to (b). (a-ii, b-ii, and b-iii) Magnified TEM images with the yellow dotted circles in a-ii and b-iii showing the regions where the d-spacings are calculated, marked as 1,2,3, and 4. The HRTEM images, along with the calculated d-spacing and its corresponding lattice planes, are shown from the regions marked 1,2,3, and 4.

Note S4

All the parameters (V_{th}, V_{hold}, t_r, G, and SERS factor) in the spider chart (Figure 6) are normalized with respect to the highest value. For example, V_{th} was the highest in the low RH conditions and was considered 1, and V_{th} in the intermediate RH, high RH, and in the O_2 atmospheres were normalized with respect to it. Similarly, other parameters were normalized with respect to the highest value. Also, the t_r and G values are taken from the data obtained with the application of 20 pulses, and at an I_{CC} of 600 μA.

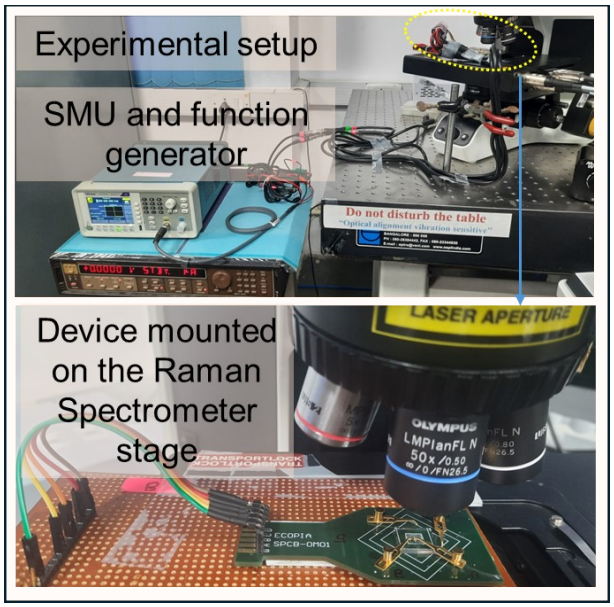

Figure S27 Photograph of the setup, showing the device on a probe card atop the Raman spectrometer stage, connected to the SMU and function generator. A magnified view of the mounted device is shown below.

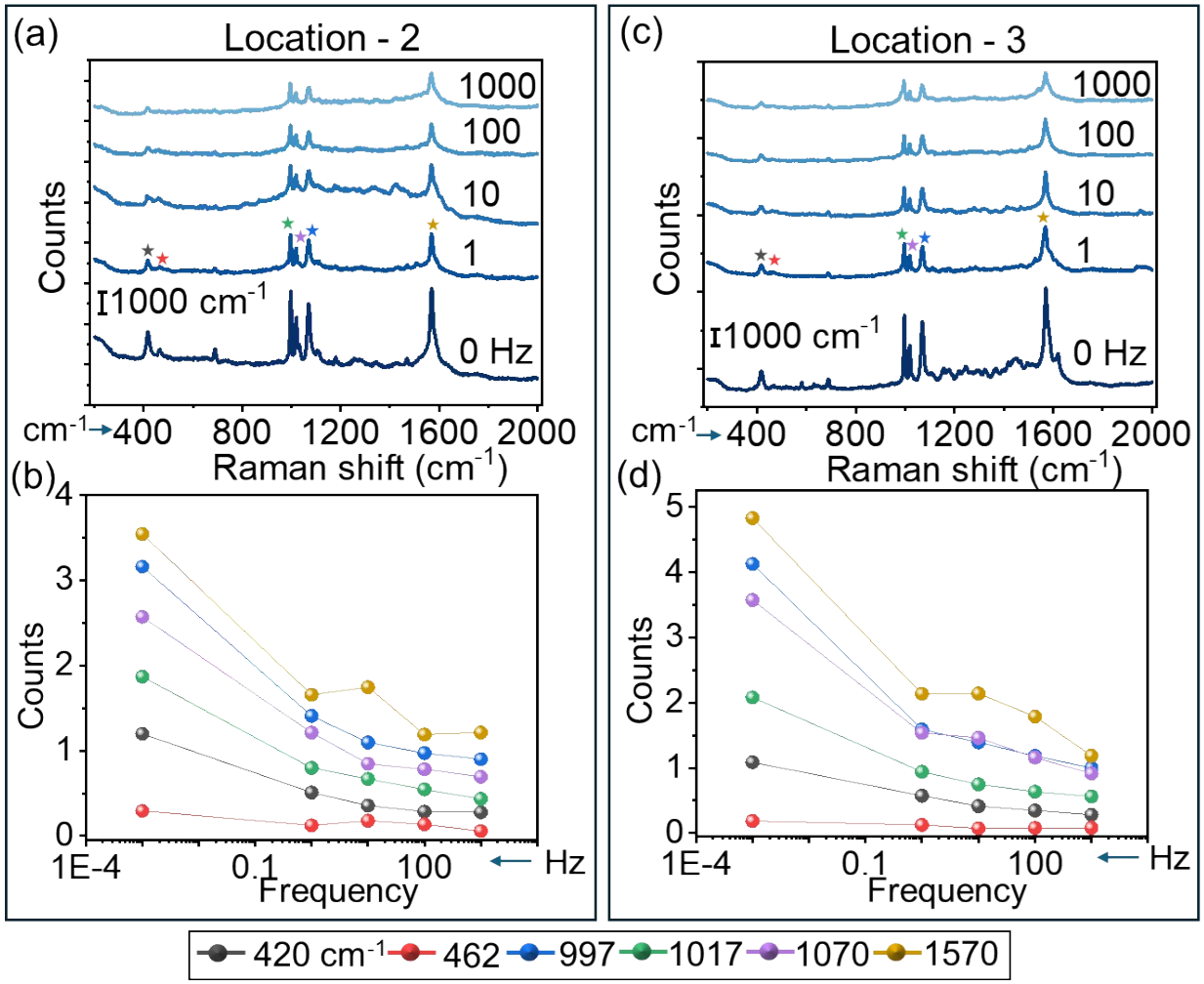

Figure S28 (a, c) Raman spectra at different locations under varying electric field frequencies, color-coded as shown at the top. Star markers indicate the color codes used for showing the variations in peak intensities corresponding to the applied electric field frequency in (b, d). (b, d) Peak intensity variation of prominent thiophenol Raman peaks with electric field frequency at different locations, color-coded as shown at the bottom.

References:

1 V. N. A. A. Samsonova, V. Dremov, O. Klimenko, N. Brilliantov, Investigation of filamentation in a-Si/Ag/Cu memristors with atomic force microscope, *arxiv Prepr.*, 2026, **arXiv:2605**, 1–13.

2 C. Hung, C. Chi, K. Hsiao and M. Lu, In Situ Scanning Transmission Electron Microscopy / Transmission Electron Microscopy Study of Defect-Driven Ag Ion Dynamics and Filament Evolution in CuO Nanowire-Based Memristors, *ACS Appl. Mater. Interfaces*, 2026, **18**, 2078–2087.

3 Q. Li, A. Diaz-Alvarez, R. Iguchi, J. Hochstetter, A. Loeffler, R. Zhu, Y. Shingaya, Z. Kuncic, K. ichi Uchida and T. Nakayama, Dynamic Electrical Pathway Tuning in Neuromorphic Nanowire Networks, *Adv. Funct. Mater.*, 2020, **30**, 2003679.

4 T. Sannicolo, D. Muñoz-Rojas, N. D. Nguyen, S. Moreau, C. Celle, J. P. Simonato, Y. Bréchet and D. Bellet, Direct Imaging of the Onset of Electrical Conduction in Silver Nanowire Networks by Infrared Thermography: Evidence of Geometrical Quantized Percolation, *Nano Lett.*, 2016, **16**, 7046–7053.

5 C. Li, T. Xu, R. Pan, S. Bao, K. Yin, J. Shen, Y. Zhu, S. Hou and L. Sun, Electric Field-Dependent Evolution Dynamics of Conductive Filaments in 2D Material-Based Planar Memristors, *ACS Nano*, 2024, **18**, 32196–32204.

6 K. Krishnan and S. Vijayaraghavan, Unraveling the Atomic Redox Process in Quantum Conductance and Synaptic Events for Neuromorphic Computing, *Adv. Electron. Mater.*, 2022, **8**, 2200509.

7 M. Pal, M. Kaur, B. Yadav, A. Bisht and G. U. Kulkarni, A Self-Formed Ag Nanostructure Based Neuromorphic Device Performing Arithmetic Computation and Area Integration: Influence of Presynaptic Pulsing Scheme on Mathematical Precision, *ACS Appl. Mater. Interfaces*, 2025, **17**, 5239–5253.

8 Tejaswini S. Rao, Ritu Gupta, and G. U. Kulkarni, Unraveling Stochastic Dynamics and Switching Mechanism in Ag Network-Based Neuromorphic Device, *Small*, 2025, **21**, 2502771.

9 Y. Yang, P. Gao, L. Li, X. Pan, S. Tappertzhofen, S. Choi, R. Waser, I. Valov and W. D. Lu, Electrochemical dynamics of nanoscale metallic inclusions in dielectrics, *Nat. Commun.*, 2014, **5**, 4232.

10 A. Cultrera, G. Milano, C. Ricciardi, L. Callegaro, I. Nazionale and M. Inrim, Mapping and Tracking Conductivity in Memristive Nanowire Networks with Electrical Resistance Tomography, *IEEE Open J. Instrum. Meas.*, 2026, 1.

11 R. Attri, I. Mondal, B. Yadav, G. U. Kulkarni and C. N. R. Rao, Neuromorphic devices realised using self-forming hierarchical Al and Ag nanostructures : towards energy-efficient and wide ranging synaptic, *Mater. Horizons*, 2024, **11**, 737–746.

12 R. Gupta, S. Siddhanta, G. Mettela, S. Chakraborty, C. Narayana and G. U. Kulkarni, Solution processed nanomanufacturing of SERS substrates with random Ag nanoholes exhibiting uniformly high enhancement factors, *RSC Adv.*, 2015, **5**, 85019–85027.